Reduced-Scale Transition-Edge Sensor Detectors for Solar and X-Ray Astrophysics

Aaron M. Datesman, Joseph S. Adams, Simon R. Bandler, Gabriele L. Betancourt-Martinez, Meng-Ping Chang, James A. Chervenak, Megan E. Eckart, Audrey E. Ewin, Fred M. Finkbeiner, Jong Yoon Ha, Richard L. Kelley, Caroline A. Kilbourne, Antoine R. Miniussi, Frederick S. Porter, John E. Sadleir, Kazuhiro Sakai, Stephen J. Smith, Nicholas A. Wakeham, Elissa H. Williams, Edward J. Wassell, and Wonsik Yoon

***Abstract*—We have developed large-format, close-packed X-ray microcalorimeter arrays fabricated on solid substrates, designed to achieve high energy resolution with count rates up to a few hundred counts per second per pixel for X-ray photon energies up to 8 keV. Our most recent arrays feature 31-micron absorbers on a 35-micron pitch, reducing the size of pixels by about a factor of two. This change will enable an instrument with significantly higher angular resolution. In order to wire out large format arrays with an increased density of smaller pixels, we have reduced the lateral size of both the microstrip wiring and the Mo/Au transition-edge sensors (TES). We report on the key physical properties of these small TESs and the fine Nb leads attached, including the critical currents and weak-link properties associated with the longitudinal proximity effect.**

***Index Terms*—Arrays, low temperature detectors, microcalorimeters, transition-edge sensors (TES), X-ray spectroscopy.**

Manuscript received September 6, 2016; accepted December 22, 2016. Date of publication January 9, 2017; date of current version February 1, 2017. This work was supported in part by NASA, Office of Space Science, from ROSES 2013 and in part by Heliophysics Technology and Instrument Development for Science under Grant NNH13ZDA001N-HTIDS.

A. M. Datesman, M. P. Chang, and E. J. Wassell are with NASA Goddard Space Flight Center, Greenbelt MD 20771 USA, and also with Stinger-Ghaffarian Technologies, Inc., Greenbelt, MD 20771 USA (e-mail: aaron.m.datesman@nasa.gov; meng-ping.chang@nasa.gov; edward.j.wassell@nasa.gov).

J. S. Adams and S. J. Smith are with NASA Goddard Space Flight Center, Greenbelt MD 20771 USA, and also with the CRESST, University of Maryland, College Park MD 20742 USA (e-mail: Joseph.S.Adams@nasa.gov; stephen.j.smith@nasa.gov).

S. R. Bandler, J. A. Chervenak, M. E. Eckart, A. E. Ewin, R. L. Kelley, C. A. Kilbourne, F. S. Porter, and J. E. Sadleir are with NASA Goddard Space Flight Center, Greenbelt MD 20771 USA (e-mail: Simon.R.Bandler@nasa.gov; James.A.Chervenak@nasa.gov; Megan.E.Eckart@nasa.gov; Audrey.E.Ewin@nasa.gov; Richard.L.Kelley@nasa.gov; Caroline.A.Kilbourne@nasa.gov; Frederick.S.Porter@nasa.gov; john.e.sadleir@nasa.gov).

G. L. Betancourt-Martinez is with NASA Goddard Space Flight Center, Greenbelt MD 20771 USA, and also with the University of Maryland, College Park MD 20742 USA (e-mail: Gabriele.L.Betancourt-Martinez@nasa.gov).

F. M. Finkbeiner is with NASA Goddard Space Flight Center, Greenbelt MD 20771 USA, and also with the Wyle Information Systems, McLean VA 22102 USA (e-mail: Fred.M.Finkbeiner@nasa.gov).

J. Y. Ha and E. H. Williams are with NASA Goddard Space Flight Center, Greenbelt MD 20771 USA, and also with the SB Microsystems Inc., Glen Burnie MD 20161 USA (e-mail: jongyoon.ha@sbmicrosystems.us; elissa@sbmicrosystems.us).

A. R. Miniussi, K. Sakai, N. A. Wakeham, and W. Yoon are with NASA Goddard Space Flight Center, Greenbelt MD 20771 USA, and also with the Universities Space Research Association, Columbia MD 21046 USA (e-mail: antoine.r.miniussi@nasa.gov; kazuhiro.sakai@nasa.gov; Nicholas.a.wakeham@nasa.gov; wonsik.yoon@nasa.gov).

Color versions of one or more of the figures in this paper are available online at http://ieeexplore.ieee.org.

Digital Object Identifier 10.1109/TASC.2017.2649839

I. Introduction

WE HAVE been developing small-pixel x-ray microcalorimeters for solar physics applications [1]–[3]. The basic requirements for this application are that the pixels are small and fast (with decay times less than a few tens of microseconds), can be fabricated into large arrays of close-packed pixels, and have a realizable read-out scheme. The previous generation featured absorbers 65 μm square on a 75 μm pitch, attached to Mo/Au bilayer transition-edge sensors (TESs) 36 $\times$ 3 μm in size. In the current generation, the pixel spacing is reduced to 35 μm, while the sensors are fabricated with dimensions as small as 7 μm across. These changes increase the areal pixel density by a factor of four while revealing device behaviors relating to the longitudinal proximity effect.

The basic geometry of these devices is depicted in Fig. 1. Each detector pixel consists of an X-ray absorber in strong thermal contact with a sensitive TES thermometer. The cantilevered absorber is supported by only a single round stem, one micron in diameter, located in the center of the TES. The transition-edge sensor is a superconducting bilayer of molybdenum and gold that can be biased in-between its superconducting and normal metal states, where any small change in temperature is transduced into a measurable current. The properties of these small TESs are determined by the dependence of the critical current on temperature, magnetic field, and size. Many of these properties have been explained by the junction-like properties of the weak link formed by the TES sensor and the superconducting leads attached, forming an S-N′-S weak-link. [4]

II. Array Designs

A key aspect to the development of compact arrays is the ability to route the fine pairs of wires carrying the TES current with high density. It requires a minimum of eight pairs of wires between each pixel at the outer edge in order to wire out all of the pixels comprising a 32 $\times$ 32 array. [5] The previous generation utilized a microstrip structure with a 4 μm pitch. [1] The widths of the lower (Lead 1) and upper (Lead 2) conductors were 2.5 μm and 1.5 μm, respectively, with a gap between lines of 1.5 μm. Using optical reduction lithography with the capability to resolve structures down to 280 nm and an overlay accuracy of 40 nm, these dimensions have now been reduced to a 2 μm pitch, with lead widths of 1 μm and 0.5 μm, producing

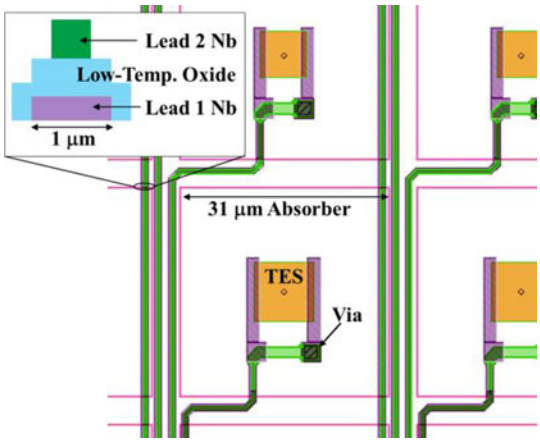

Fig. 1. Schematic of the small pixel array design showing TESs with microstripped leads, vias, stems, and 31 μm absorbers. Inset: microstrip structure in cross-section.

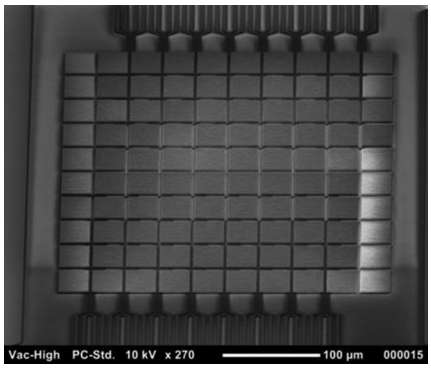

Fig. 2. 10 $\times$ 10 absorber-coupled TES array with 2 μm thick absorbers on single stems 1 μm in diameter.

a 1 μm gap. The reduced scale would suffice to wire out a 48 $\times$ 48 array on a 35 μm pitch, exceeding 2300 total pixels. A single detector chip contains 64 wired-out sensors with four TES dimensions: 7, 8, 9, and 12 μm. The 10 $\times$ 10 test array is shown in Fig. 2.

The absorbers are electroplated gold 31 $\times$ 31 $\times$ 2 μm, with a gap between absorbers of 4 μm. Future development will focus on increasing the thickness to 4 μm. In these prototype detectors there are no normal metal banks along the two edges between the TES contacts, and also no normal metal stripes such as have been empirically shown to reduce unexplained detector noise in larger TESs [6]. The absence of these features simplifies the analysis of experimental results. The array, although deposited on a silicon wafer covered with layers of thermal oxide and low-stress LPCVD silicon nitride, has not been released and sits on a solid substrate rather than on a membrane. There is also no embedded heat sink layer, which is typically employed to reduce thermal cross-talk between pixels [7]. In future we will use a back-etch to make the membranes underneath the pixels free-standing, and then deposit a film of copper onto the backside of the chip to provide the heat bath, as has been employed in some other prototype arrays [8].

We discuss in this report results from two fabrication runs. Example TESs from each run, denoted "A" and "B", are shown

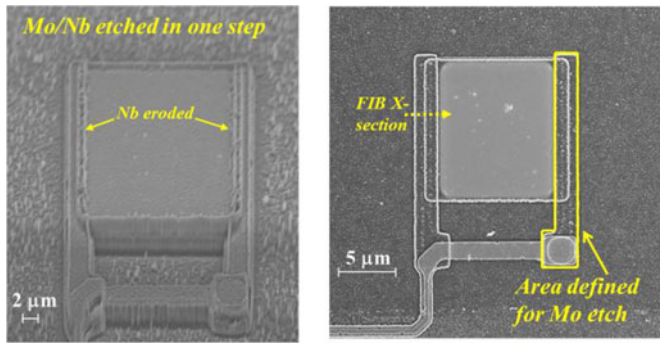

Fig. 3. (a) Completed TES device "A". The Nb leads are eroded and overlap the TES by less than 0.5 μm on each side. The TES is covered by a layer of low-temperature deposited silicon dioxide. (b) Completed TES device similar to "B". The Nb leads overlap the TES by a full 1 μm, as designed; the SiO_x layer has been removed.

in Fig. 3. The "B" fabrication process included cantilevered absorbers, while for "A" it did not. Results from testing of these devices suggest differences in the interface structure and geometry between the Mo/Nb leads and the Mo/Au TESs, described in the next section.

III. Fabrication

The devices are fabricated on a silicon wafer 300 μm thick, coated with layers of thermal silicon dioxide and low-stress LPCVD silicon nitride. The Mo/Au (approximately 50 nm/220 nm) bilayer is removed from the wafer perimeter using a wet etch to facilitate the subsequent patterning and etching of alignment marks for optical reduction lithography. The Mo/Au TESs, 7–12 μm in size, are patterned by optical reduction lithography and etched by argon ion milling. By simple timing it is possible in the load-locked ion mill system to reliably remove the gold layer while halting only partway through the molybdenum layer below. The "A" and "B" fabrication processes diverged at this point. For "A", deposition of the 200 nm thick Lead 1 Nb layer followed next. It was therefore necessary for the reactive ion etch (RIE) defining Lead 1 to remove the Nb and Mo layers together, under the same photoresist mask. The etch slowed on the Mo layer, requiring a significant over-etch that eroded the niobium layer on top of the TES. This issue was addressed for "B" by patterning the Mo layer to define and remove regions adjacent to the TES prior to Lead 1 deposition, as indicated in Fig. 3(b).

A focused-ion beam (FIB) cross-section of side-by-side completed microstrip structures from "B" is shown in Fig. 4(a). Registration between the Lead 1 and Lead 2 layers is consistent with the 40 nm overlay specification. Measurement reveals critical currents for the Mo/Au bilayer of 548 μA at 475 mK and 960 μA at 200 mK, which exceeds the operational requirement by a significant margin. The critical current density in the Lead 2 layer therefore exceeds 1.0 $\times$ 10^6 A/ cm^2.

The cantilevered absorbers are fabricated using seed layer deposition over a photoresist layer defining the absorber "stems", followed by plating and ion milling to define the absorber "hood". Success requires that the photoresist mold for the stem have a sloped, positive profile. While this may be achieved by

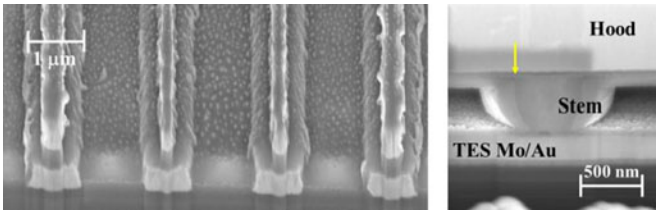

Fig. 4. FIB cross-sections: (a) Microstrip structures with 1 μm and 0.5 μm (nominal) lower and upper conductors, separated by a 300 nm thick dielectric layer. (b) Cantilevered absorber with a 1 μm diameter stem, fabricated using a defocus setting of -1.36 μm. The interface between the evaporated and plated gold layers in the stem is indicated with an arrow.

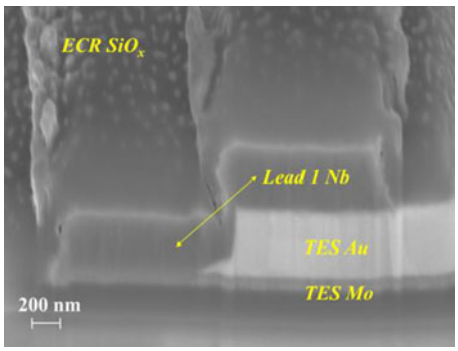

Fig. 5. FIB cross-section of the TES-lead interface for a "B" device.

reflowing the photoresist at an elevated temperature, the approach is not suitable at stem dimensions of 1 μm and smaller. We employed an alternative approach for "B" in which the mask image of the stem is slightly defocused during exposure using optical reduction lithography. The method has been demonstrated to create a sloped resist profile. [9] A matrix of defocus settings between -5.0 μm and $+5.0$ μm was explored to select the proper value for this application by trial and error. Values between -0.80 μm and -1.36 μm were identified as promising; absorber test structures with stems as small as 0.75 μm yielded successfully. Fig. 4(b) shows the cross-section of an absorber fabricated using this approach.

IV. Interface Characterization

In Fig. 5 we present an FIB cross-section of the TES-lead interface for a "B" device. The Lead 1 niobium layer overlapping the TES is whole, undamaged, and in good contact with both the gold underneath it and with the adjacent Mo/Nb lead. The overlap dimension is 1 μm, so that the lead spacing L is two microns less than the TES dimension. The edge of the TES is somewhat sloped, which is desirable for step coverage, with a tail extending about 200 nm underneath Lead 1. At the edge of the lead, the niobium structure is aligned very well to the molybdenum layer, which was patterned and etched in a separate step. In profile, the Lead 1 niobium is nicely sloped. A positive profile is necessary for fabrication of a high-quality via. In summary, the fabrication process yields the desired physical structure, with excellent size resolution and overlay.

Examination of the "A" devices reveals that the niobium on top of the TES gold is eroded, as indicated by the image of Fig. 3(a). Therefore the lead spacing for "A" devices is only one micron less than the TES dimension. The "A" devices nevertheless exhibit good Mo-Nb contact in the lead, with a sloped TES sidewall.

TABLE I
Transition Temperature Measurements

Lead Spacing L (μm)	"A" T_C (mK)	"B" T_C (mK)
5		>1200, $>1200^*$
6	460, 480	1000, 1050, $>1200^*$
7	530, 560	>1200
8	370, 370	
10		790
11	260	
T_{Ci} (mK)	164	84
R_{TES} (mΩ)	27	12.5

Table 1 Transition temperature measurements under 10 μA excitation for "A" and "B" devices. T_{Ci} is the intrinsic transition temperature of the Mo/Au bilayer material. "B" measurements on a device with no absorber are denoted with an asterisk.*

V. Electrical Characterization

Table 1 shows measurements of the transition temperature (T_C) for "A" and "B" devices. T_C indicates the beginning of the superconducting transition as measured using SQUID electronics while slowly increasing the base temperature. The applied bias is a 10 μA triangular wave with a frequency of 2 Hz. Seven devices were tested from both "A" and "B" fabrication runs, each covering all four sizes of TES devices. Two devices from "B" had no absorbers. The intrinsic transition temperature of the Mo/Au bilayer material was 164 mK for "A" and 84 mK for "B", in each case measured on a Mo/Au test structure using a four-wire method.

Device normal resistances were approximately 27 mΩ and 12.5 mΩ, respectively. Due to the longitudinal proximity effect, the niobium leads sustain superconductivity in the Mo/Au TES far above the intrinsic transition temperature (T_{ci}) exhibited by the bilayer. The effect is found for both "A" and "B". The effect is smaller for "A" either due to erosion of the niobium lead where it overlaps the TES, or because of the higher normal state resistance of the TES bilayer.

The data indicate that the T_C enhancement does not decline monotonically with lead spacing. For both "A" and "B", devices with L = 7 μm exhibited a higher critical temperature than devices with L = 6 μm lead spacing. An explanation for this observation is currently lacking. There also appears to be a meaningful discrepancy between the critical temperature measured for "B" devices with and without absorbers, which is attributable to the effect of the absorber stem in contact with the TES surface.

The critical current as a function of temperature for a 7 μm device from "B" (L = 5 μm), a 7 μm device from "A" (L = 6 μm), and previously published data from a TES device of a different design with 8 μm lead spacing [4] is plotted in Fig. 6. The published data has been shown to fit well to a theory derived from the Ginzburg-Landau equations, exhibiting an exponential dependence on L. The data from an "A" device correspond reasonably closely to the previously published data, which is expected since the values of the intrinsic transition temperature

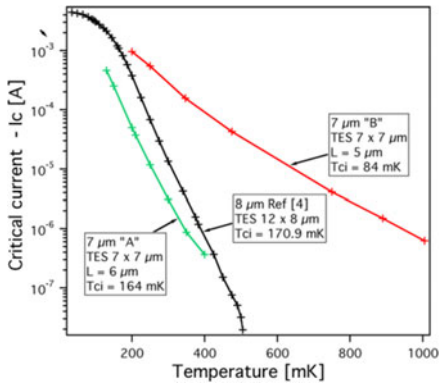

Fig. 6. Critical currents of "A" and "B" devices compared to a previous result for an L = 8 μm TES device. [4] None of the devices have absorbers.

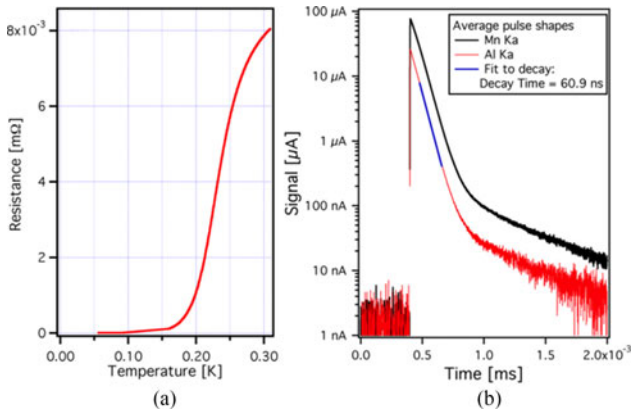

Fig. 7. (a) Resistance verses temperature curve for a 12 μm device (L = 10 μm), and (b) pulse shapes for 1.5 and 5.9 keV X-rays, measured using a 9 μm TES (L = 7 μm) with a 31 μm absorber, both at a bath temperature of 55 mK.

(170.9 mK vs. 164 mK) and lead spacing are very similar. At 60 mK, the L = 6 μm "A" device exhibits $I_C = 0.95$ mA; for the L = 5 μm "B" device, $I_C = 5.7$ mA at 55 mK. Compared to the "A" device, it is clear that the "B" device exhibits a much greater critical current over a broad temperature range.

VI. X-ray Microcalorimeter Performance

We have made first measurements of a "B" pixel as an X-ray microcalorimeter using a 9 μm TES (L = 7 μm). Devices of other dimensions have not yet been tested. The resistance versus temperature curve under test conditions for a bath temperature of 55 mK is shown in Fig. 7(a). It was determined from an I-V measurement of the TES, assuming that the thermal conductance is given by the thermal boundary resistance as calculated by Lee *et al.* [10]. The normal resistance was 12.5 mΩ. The TES was then biased at 2.5% of the TES normal resistance (0.31 mΩ). The energy sensitivity was determined from the average signal response to 1.5 keV Al Kα X-rays, measuring the average noise spectrum and then integrating the noise equivalent power [11].

As can be seen in Fig. 7(b), the signal for the AlKα X-rays has a single exponential decay for most of the pulse, followed by a second longer decay of low amplitude. The first decay time constant is 60 ns. The second decay is likely related to a

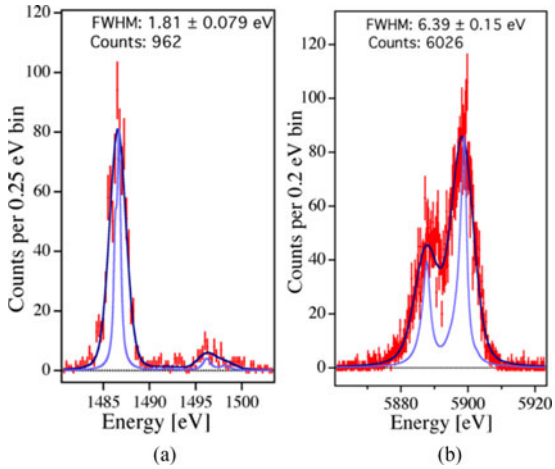

Fig. 8. Measured energy spectrum of (a) Al Kα complex and (b) Mn Kα complex. The dark blue curves are the best fits to the spectrum, and the light blue curves are the line shapes used.

small amount of heating of the substrate since this first prototype detector does not yet incorporate a layer of heat-sinking copper underneath it, separated by an insulation layer. The signals from 6 keV X-rays only show a small amount of non-linearity even though the temperature rise from these X-rays is expected to be approximately 30 mK, since the 31 μm absorber is just 2 μm thick.

Spectra acquired from two different energies, and from two different X-ray sources are shown in Fig. 8(a) and (b). Fig. 8(a) shows a measurement of fluorescent Al Kα X-rays from a Manson source. The energy resolution achieved corresponds to the broadening of the intrinsic Al Kα X-rays by a microcalorimeter energy resolution of 1.8 eV (FWHM), consistent with best achievable resolution.

Fig. 8(b) shows worse energy resolution for Mn Kα X-rays from an ^{55}Fe radioactive source of around 6.4 eV (FWHM). The origin of this broadening is not yet understood. Possibly it arises because the prototype device has a thin absorber, which thermalizes slowly compared to the fast pulse decay time. Athermal phonon loss is not expected to be a problem [12] because the area of the contact region between the absorber and the TES is only $\sim$0.1%, far less than has previously been shown to be needed for athermal phonon loss to be a problem at this resolving power [13].

VII. Conclusion

We have developed the first X-ray microcalorimeter arrays on a pitch as fine 35 μm. The basic design and operation was successful, demonstrating the high potential for this type of X-ray microcalorimeter for future solar and X-ray astrophysics instruments. The new fabrication techniques used to create extremely fine-pitch microstrip lines, the very small TESs, and the attachment of absorbers through 1 μm stems, have all successfully been demonstrated for the first time. Measurements indicate that the TES properties appear highly dependent on the interface geometry between the TES and its leads.

REFERENCES

[1] S. R. Bandler *et al.*, "Advances in small pixel TES-based X-ray microcalorimeter arrays for solar physics and astrophysics," *IEEE Trans. Appl. Supercond.*, vol. 23, no. 3, Jun. 2013, Art. no. 2100705, doi: 10.1109/TASC.2013.223.

[2] S. R. Bandler *et al.*, "Society of photo- optical instrumentation engineers (SPIE) conference series," in *Proc. SPIE*, 2010, vol. 7732, Art. no. 773238.

[3] J. M. Laming *et al.*, "Science objectives for an x-ray microcalorimeter observing the sun," ArXiv e-prints, 2010, arXiv:1011.40522010.

[4] J. E. Sadleir, S. J. Smith, S. R. Bandler, J. A. Chervenak, and J. R. Clem, "Longitudinal proximity effects in superconducting transition-edge sensors," *Phys. Rev. Lett.*, vol. 104, no. 4, Jan. 2010, Art. no. 047003.

[5] J. A. Chervenak *et al.*, "Fabrication of microstripline wiring for large format transition edge sensor arrays," *J. Low Temp. Phys.*, vol. 167, no. 3–4, pp. 547–53, May 2012.

[6] S. J. Smith *et al.*, "Implications of weak-link behavior on the performance of Mo/Au bilayer transition-edge sensors," *J. Appl. Phys.* vol. 114, 2013, Art. no. 074513, doi: 10.1063/1.4818917.

[7] F. M. Finkbeiner *et al.*, "Development of embedded heatsinking layers for compact arrays of X-ray TES mi- crocalorimeters," *IEEE Trans. Appl. Supercond.* vol. 21, no. 3, pp. 223–226, Jun. 2011.

[8] W. Yoon *et al.*, "Design and performance of hybrid arrays of Mo/Au bilayer transition-edge sensors," In *Proc. IEEE Trans. App. Supercond.*, 2016, doi: 10.1109/TASC.2017.2655718.

[9] J. Riege, S. Mony, and N. Ebrahimi, "A new method for creating sloped resist profiles using mask structures," Skyworks Solutions, Inc., Newbury Park, CA, USA, White Paper.

[10] S.-J. Lee *et al.*, "Fine pitch transition-edge sensor X-ray microcalorimeters with sub-eV energy resolution at 1.5 keV," *App. Phys. Lett.* vol. 107, 2015, Art. no. 223503, doi: 10.1063/1.4936793.

[11] D. McCammon, "Thermal equilibrium calorimeters: an introduction," in *Cryogenic Particle Detection* (vol. 99 of Topics in Applied Physics), C. Enss, Ed., New York, NY, USA: Springer-Verlag, 2005, pp. 1–34.

[12] A. G. Kozorezov *et al.*, "Athermal energy loss from x-rays deposited in thin superconducting films on solid substrates," *Phys. Rev. B*, vol. 87, 2013, Art. no. 104504.

[13] S. J. Smith *et al.*, "Small pitch transition-edge sensors with broadband high spectral resolution for solar physics," *J. Low. Temp. Phys.*, vol. 167, pp. 168–175, Feb. 2012.